INORGANIC
CHEMISTRY
FRONTIERS

RESEARCH ARTICLE

Check for updates

Europium doped-double sodium bismuth molybdate nanoparticles as contrast agents for luminescence bioimaging and X-ray computed tomography†

Roxana M. Calderón-Olvera, [ID] [a] Nuria O. Núñez, [ID] [a] Daniel González-Mancebo, [a] Jose M. Monje-Moreno, [ID] [b] Manuel J. Muñoz-Rui,[b] Elisabet Gómez-González, [ID] [a] Encarnación Arroyo, [ID] [a] Beatriz Torres-Herrero, [ID] [c] Jesús M. de la Fuente[c] and Manuel Ocaña [ID] *[a]

A one-pot method for the synthesis of uniform Eu^{3+}-doped $NaBi(MoO_4)_2$ nanoparticles with an ellipsoidal shape and tetragonal crystal structure functionalized with polyacrylic acid is reported for the first time in the literature. The method is based on a homogeneous precipitation reaction from solutions in an ethylene glycol/water medium containing appropriate bismuth, sodium, and molybdate precursors and polyacrylic acid. The luminescence properties (excitation and emission spectra and luminescence lifetime) of such nanoparticles are evaluated for different Eu^{3+} doping levels, finding an intense red emission for all synthesized samples. The X-ray attenuation properties of the nanoparticles have been also analyzed, which were found to be better than those of a commercially computed tomography contrast agent (iohexol). The dispersibility of the nanoparticles in a physiological medium was also analyzed, finding that they could be well dispersed in a 2-*N*-morpholinoethanesulfonic acid monohydrate medium (pH = 6.5). Finally, the cell viability of such a phosphor has been analyzed using MIA-PaCa-2 cells and its *in vivo* toxicity has been evaluated using the nematode *Caenorhabditis elegans* model finding no significant toxicity in both cases up to a nanoparticle concentration of 100 μg mL^{-1}, which is within the range required for most *in vivo* applications. The developed Eu^{3+}-doped $NaBi(MoO_4)_2$ nanoparticles are, therefore, excellent candidates for their use as bimodal probes for luminescence imaging and X-ray computed tomography.

1. Introduction

Lanthanide (Ln)-doped double sodium rare-earth (RE) molybdates ($NaRE(MoO_4)_2$) have been the subject of increasing interest during the last few years due to their interesting luminescence properties, which make them useful for many applications in different fields such as catalysis,[1] lighting,[2–4] thermometry,[5] ionic conductivity,[6] and bioimaging.[7,8] Focusing on the latter application, the high atomic number (Z) of Ln confers to the $NaRE(MoO_4)_2$ compounds a strong capacity for X-ray attenuation.[9] Because of this characteristic, such materials have been investigated as dual contrast agents (CAs) for both luminescence and computed tomography (CT) imaging.[10] Since the X-ray adsorption coefficient increases with Z^4,[9] the higher the Z of the elements constituting the CA, the better the performance of the latter for CT imaging. Therefore, CAs based on double sodium bismuth molybdate ($NaBi(MoO_4)_2$), which shows a similar composition and structure to $NaRE(MoO_4)_2$, would be excellent probes for CT owing to the much higher Z value for Bi (83) than for Ln (57–71). In fact, the good performance of other bismuth-based nanomaterials (oxides, sulphides, fluorides), as CT contrast agents, has been reported.[11] Despite this perspective, the potentiality of Ln-doped $NaBi(MoO_4)_2$ has never been reported to the best of our knowledge. This might be due to the lack of synthesis methods suitable to produce particles with the characteristics required for *in vivo* bioapplications, which include a uniform shape, narrow size distribution within the nanometer range, dispersibility in physiological media, and biocompatibility. In fact, most reported procedures for the preparation of NaBi

[a]*Instituto de Ciencia de Materiales de Sevilla (CSIC-Universidad de Sevilla), c/ Américo Vespucio, 49, 41092 Sevilla, Spain. E-mail: mjurado@icmse.csic.es*
[b]*Centro Andaluz de Biología del Desarrollo (CABD), Universidad Pablo de Olavide (UPO), Molecular Biology and Biochemical Engineering Department, CSIC/UPO/JA, Carretera de Utrera Km1, 41013-Sevilla, Spain*
[c]*Instituto de Nanociencia y Materiales de Aragón (CSIC-Universidad de Zaragoza) and CIBER-BBN, Edificio I+D, C/Mariano Esquillor s/n, 50018 Zaragoza, Spain*
†Electronic supplementary information (ESI) available. See DOI: https://doi.org/10.1039/d2qi02664c

3202 | *Inorg. Chem. Front.*, 2023, **10**, 3202–3212

This journal is © the Partner Organisations 2023

$(MoO_4)_2$-based phosphors involve solid-state reactions,[12,13] coprecipitation,[14–16] or sol-combustion methods,[17] yielding particles with a heterogeneous size and shape and in most cases, a high aggregation degree.

In this paper, a method for the synthesis of uniform Eu^{3+}-doped $NaBi(MoO_4)_2$ nanoparticles (NPs) functionalized with polyacrylic acid (PAA) is reported for the first time in the literature. Here, Eu^{3+} cations were selected as dopants as a proof of concept and also because they can be efficiently excited by visible radiation,[14] thus enabling bioimaging using a confocal microscope. PAA was chosen for functionalization since it has been widely shown that its carboxylate groups can be strongly coordinated to the surface of many NP-based bioprobes, which confer to them a high dispersibility in aqueous media and biocompatibility.[18] To assess the suitability of such NPs as dual probes for luminescence and CT imaging, the luminescence properties of such NPs are first evaluated and optimized by varying the Eu^{3+} doping level. Then, the X-ray attenuation properties and dispersibility in a physiological pH simulator medium (2-*N*-morpholinoethanesulfonic acid monohydrate) of the optimum nanophosphor are analyzed. Finally, the cell viability of such a phosphor is analyzed and its *in vivo* toxicity is evaluated using the nematode *Caenorhabditis elegans* (*C. elegans*), which has been known to be an adequate animal model for the evaluation of interactions between NPs and biological systems.[19,20]

2. Experimental

2.1. Reagents

Bismuth(III) nitrate pentahydrate ($Bi(NO_3)_3·5H_2O$, Sigma-Aldrich, 99.99%) and europium(III) nitrate pentahydrate ($Eu(NO_3)_3·5H_2O$, Sigma-Aldrich, 99.9%) were selected as cation precursors and sodium molybdate (Na_2MoO_4, Sigma-Aldrich, ≥98%) as the sodium and molybdate source. A mixture of ethylene glycol (EG, Sigma-Aldrich, ≥99.5%) with water (Milli-Q) was used as the solvent, and poly(acrylic acid) (PAA, Sigma-Aldrich, average $M_W \sim 1800$) was employed for the functionalization of the nanoparticles. The colloidal stability study was conducted using 2-*N*-morpholinoethanesulfonic acid monohydrate (MES, Sigma-Aldrich, ≥99%) as a simulator of physiological pH. Iohexol (≥95%, Sigma-Aldrich), a commercial CT contrast agent, was used for comparative purposes.

For cytotoxicity evaluation, MIA PaCa-2 cells (ATCC), Advanced Dulbecco's Modified Eagle Medium (DMEM; Gibco®, Fisher Scientific), fetal bovine serum (FBS, BioWhittaker™), glutaMAX™, penicillin/streptomycin (Gibco®, Fisher Scientific), Triton X-100 (Sigma-Aldrich), (3-(4,5-dimethylthiazol-2-yl)-2,5-diphenyltetrazolium bromide (MTT; Molecular Probes) and dimethyl sulfoxide (DMSO; Sigma-Aldrich) were used.

2.2. *Caenorhabditis elegans* strains and maintenance conditions

Caenorhabditis elegans Bristol strain N2 and *Escherichia coli* OP50 were obtained from the Caenorhabditis Genetic Canter (CGC) stock collection, University of Minnesota, St Paul, MN, USA. Nematode growth medium (NGM) and M9 Buffer (M9) were prepared as previously described.[21] NGM plates were seeded with OP50 as a food source and the experimental temperature was set at 20 °C.

2.3. Synthesis of undoped $NaBi(MoO_4)_2$@PAA nanoparticles

$NaBi(MoO_4)_2$ nanoparticles functionalized with PAA were synthesized according to a procedure previously developed by us for the preparation of $NaLa(MoO_4)_2$ nanoparticles,[10] which was adapted to produce uniform nanoparticles of the desired compound by introducing slight modifications. Essentially, it consisted of a homogenous precipitation process from solutions containing appropriate precursors using a mixture of EG/water as the solvent. The selected composition for this mixture was 4/1 (volumetric ratio) since, as it was shown in our previous work on $NaLa(MoO_4)_2$, in pure EG, irregular and aggregated particles were obtained, whereas NPs with a mean size above the nanometer range resulted when using a higher water content.[10] This behavior was attributed to the differences in the viscosity and dielectric constant of the solvent when varying the amount of EG in the mixture, and this has a strong influence on the precipitation kinetics and consequently on the particle size and shape.[10] The experimental procedure was as follows. The required amount (0.04 M) of the bismuth precursor was dissolved in EG (2.5 mL), whereas the molybdate precursor (0.1 M) was dissolved in an EG/water mixture (1.5 mL EG + 1 mL water). The PAA polymer (2 mg mL^{-1}) was added to the latter solution. After the homogenization of the reagents, both solutions were admixed and the resulting mixture (total volume = 5 mL) was aged for 20 h in an oven at 120 °C. The obtained dispersion was cooled down to room temperature, centrifuged to remove the supernatant, and washed twice with ethanol and three times with distilled water. The so-prepared nanoparticles were stored in Milli-Q water dispersions. When required they were dried at room temperature.

2.4. Synthesis of Eu-doped $NaBi(MoO_4)_2$@PAA nanoparticles

Eu^{3+}-doped $NaBi(MoO_4)_2$@PAA nanoparticles having different Eu^{3+} contents (5, 10, 20, and 30%, expressed as the Eu/Eu + Bi molar ratio) were synthesized according to a procedure previously described, adding the desired amount of europium nitrate to the initial bismuth nitrate solution. In all cases, the other experimental parameters were kept constant, including the total concentration of cations (0.04 M).

2.5. Characterization

Transmission electron micrographs (TEM) were recorded using a JEOL 2100Plus, 200 kV microscope. Particle size distributions were estimated from the TEM micrographs by counting hundreds of particles using the free ImageJ software.

The dispersibility of the nanoparticles (0.5 mg mL^{-1}) in water and MES solution (50 mM at pH = 6.5) was evaluated by estimating their hydrodynamic diameter (HD) from dynamic

This journal is © the Partner Organisations 2023

Inorg. Chem. Front., 2023, **10**, 3202–3212 | **3203**

light scattering (DLS) measurements conducted in a Zetasizer NanoZS90, Malvern instrument.

X-ray diffraction (XRD) patterns were recorded on a Panalytical X'Pert Pro diffractometer using a step of 0.02° (2θ) and 1000 s of accumulation time. Unit cell parameters were calculated by Rietveld refinement of the XRD data using the X'Pert High Score Plus software. The starting structural parameters were taken from the work of Waskowska *et al.*[22] for undoped $NaBi(MoO_4)_2$.

Fourier transform infrared spectra (FTIR) were recorded on a JASCO FT/IR-6200 apparatus using the samples diluted in KBr pellets and thermogravimetric analyses (TGA) were conducted using a Q600 TA instrument, at a heating rate of 10 °C min^{-1} in air.

Excitation and emission spectra of the samples dispersed in Milli-Q water (5 mg mL^{-1}) were recorded using a spectrofluorometer (Fluorolog FL3-11) equipped with a Xenon CW lamp of 450 W operating in the front face mode. The same equipment was used for lifetime measurements by exciting the dried samples at 465 nm and recording the luminescence decay at an emission wavelength of 614 nm.

A Zeiss Xradia 610 Versa 3D X-ray microscope (XRM) was used to measure the capability for X-ray attenuation of aqueous dispersions of the nanoparticles as well as of an iohexol solution (commercial CT CA). Different concentrations of each sample were placed in 2.0 mL Eppendorf tubes to obtain the X-ray absorption values. Acquisition parameters were 123 μA current, 70 kVp voltage, and 0.1 s of exposure time. The objective used was 0.4×, without any filter, obtaining a pixel size of 213 μm. Image reconstruction was done using Reconstructor Scout and Scan 16.1.13.038 software using 801 projections. The final images were analyzed using open source software (ImageJ), using a spherical volume of 0.5 cm radius, to calculate the X-ray attenuation in Hounsfield units (HU). Air (−1000 HU) and water (0 HU) were employed to calibrate the final images.

2.6. Cytotoxicity evaluation

2.6.1 MTT assay. *In vitro* cell viability was assessed by the MTT assay[23] using the human pancreatic ductal adenocarcinoma cell line MIA-PaCa-2, as described in our previous paper.[24] Cells were cultured at 37 °C under a 5% CO_2 atmosphere in DMEM supplemented with 10% FBS, 2 mM glutaMAXTM, and 100 U mL^{-1} of penicillin/streptomycin. Essentially, the procedure was as follows. MIA-PaCa-2 cells were seeded at a density of 10 000 cells per well in 96 well plates and incubated for 24 h under cell culture standard conditions. Afterward, NPs at different concentrations, from 125 to 8 μg mL^{-1}, were added to the cells and further incubated for 24 h. Each procedure was performed in triplicate. After exposure, the cells were washed with PBS. Then, 100 μL of a 0.5 mg mL^{-1} MTT solution was added and incubated light-protected under culture conditions for 45 min. As death control (positive control), a 0.5% solution of Triton X-100 was added prior to MTT addition. Well plates were centrifuged for 20 min (1250 rpm) and 100 μL DMSO was added

to dissolve formazan crystals. After homogenization for 15 min at 37 °C under constant agitation, the absorbance intensity at 540 nm was recorded using a Multiskan™ FC Microplate photometer. Untreated cells were used as the negative control. Viability was determined with respect to the untreated cells.

2.6.2 Cell morphology. Changes in cell morphology were evaluated by optical microscopy. Similarly to the MTT assay, MIA PaCa-2 cells were seeded at a density of 10 000 cells per well in a 96-well plate and incubated for 24 h. The cells were exposed to NPs in varying concentrations ranging from 125 to 8 μg mL^{-1}. After 24 h of incubation, the cells were washed with PBS. Cell morphology images were acquired using a Nikon Eclipse TE2000-S. Three well replicas for each condition were analyzed by capturing brightfield images in random fields per well.

2.7. *In vivo* toxicity

2.7.1. Exposure of *C. elegans* to Eu-doped NaBi $(MoO_4)_2$@PAA. Age-synchronized young larvae (L1) were obtained through the bleaching treatment of gravid adults for 24 h on M9 at 20 °C in agitation. Around 300 L1s were seeded per plate in several plates. They were grown until reaching the young adult state (approximately 52 h at 20 °C). Then, they were recovered with fresh Milli-Q water and washed three times. The worms were exposed to NPs diluted in Milli-Q water to different final concentrations and left for 24 h under agitation at 20 °C.

2.7.2. Biodistribution assay. The treated worms were washed three times with Milli-Q water and anesthetized with Levamisol 10 μM, mounted on a glass slide with aqueous mounting medium, and observed under a confocal microscope (Leica Stellaris 8 STED with an HC PL APO CS2 63×/1.40 oil objective), using white laser light to excite at 465 nm and a HyD detector (600–625 nm).

2.7.3. Toxicological assays. For the survival assay, the animals were treated with Milli-Q water (untreated worms/control) or with different concentrations of Eu-doped NaBi $(MoO_4)_2$@PAA in Milli-Q water (treated worms) in 96-well plates for 24 h, 48 wells per condition, and 100 μL per well. The assay was performed, at least, in triplicate. The plates were tapped and the worms that moved were counted as alive. In case of doubt, the worms were touched with a picking needle. Each well contained between 10 to 20 adult worms. The results are expressed as a percentage of alive worms with respect to the untreated (control) worms.

3. Results and discussion

3.1. NP synthesis and characterization

To establish the experimental conditions required for the synthesis of Eu^{3+}-doped $NaBi(MoO_4)_2$ NPs, we first addressed the undoped system for simplicity. The NPs obtained by homogeneous precipitation from $Bi(NO_3)_3$ and Na_2MoO_4 in an EG/water mixture, as described in the Experimental section, are

3204 | *Inorg. Chem. Front.*, 2023, **10**, 3202–3212

This journal is © the Partner Organisations 2023

Fig. 1 (a) TEM image, (b) particle size (length and width) histogram, (c) DLS curves in Milli-Q water, (d) X-ray diffraction patterns, (e) FTIR spectrum, and (f) TGA curve of the particles synthesized by aging at 120 °C for 20 h; solutions containing 0.04 M $Bi(NO_3)_3$, 0.1 M Na_2MoO_4, and a 2 mg mL^{-1} EG/water (4/1 by vol.) mixed solvent.

illustrated in the TEM micrograph as shown in Fig. 1a. As observed, they presented an ellipsoidal shape having a mean length of 218 nm (standard deviation, σ = 33) and a width of 75 nm (σ = 11) (Fig. 1b). The hydrodynamic diameter (HD) value (190 nm, polydispersity index, PDI = 0.1) obtained from DLS measurements (Fig. 1c) for aqueous suspensions (native pH = 6) of such NPs was in between those corresponding to their length and width, indicating that the NPs were well dispersed. They consisted of tetragonal (space group $I4_1/a$) NaBi$(MoO_4)_2$ (PDF file: 00-051-1508) according to XRD (Fig. 1d) and contained PAA molecules most probably adsorbed on their surface, as revealed by the presence of absorption bands in the 1250–1500 cm^{-1} region of their FTIR spectrum (Fig. 1e), which are attributed to the PAA carboxylate anions.[25] The amount of such organic species was quantified by TGA. Thus, the TG curve obtained for this sample showed a weight loss of 0.9% in the 25–250 °C range due to the release of adsorbed water molecules, followed by a more pronounced loss (3.1%) which took place between 250 and 350 °C, associated with the decomposition of PAA molecules (Fig. 1f).

Given the success of the synthesis process for undoped NPs, we proceeded to synthesize several samples containing different Eu^{3+} contents (5, 10, 20, and 30%, expressed as the

Eu/Eu + Bi molar ratio) to further investigate the effect of this parameter on the luminescence of NPs. For such a purpose, we used the same procedure as for the undoped system but added the desired amounts of the Eu^{3+} precursor (Eu$(NO_3)_3$) to the starting solutions. TEM pictures corresponding to the doped samples are shown in Fig. 2. They revealed that whereas the doping process did not affect the particle shape, a progressive decrease of their size from 218 × 75 nm (Fig. 1c) to 39 × 19 nm (Fig. S1†) and their HD values (Fig. S2†) from 190 to 55 nm were observed on increasing the Eu^{3+} doping level from 0 to 30% (Table 1). In agreement, we also detected (Table 1) a progressive decrease in the crystallite size obtained for the doped samples using the Scherrer formula and in the width of the most intense peak of their XRD patterns, which only showed the reflections corresponding to the tetragonal NaBi$(MoO_4)_2$ phase (Fig. S3†). This kind of effect of Ln^{3+} doping on the particle size has been previously observed and attributed to the differences between the precipitation kinetics of the doping and matrix cations, Eu^{3+} and Bi^{3+} in this case, and/or the variations of the unit cell volume induced by the incorporation of the doping cations to the host matrix.[26] Such incorporation was confirmed through the evaluation of the unit cell parameters of our doped samples obtained by Rietveld refinement of their XRD pattern (Fig. S4†). As observed in Table 1, a contraction of the unit cell (from 325.39 to 322.83 Å^3) was detected on increasing the doping level (from 0 to 30%), confirming the successful incorporation of the Eu^{3+} cations to the NaBi$(MoO_4)_2$ lattice, in agreement with the smaller size of the former cations (1.066 Å) as compared with that of Bi^{3+} (1.17 Å). A uniform Eu^{3+} distribution within the lattice was also revealed by an EDX elemental mapping analysis conducted for a single particle of the sample doped with 20% Eu^{3+} (Fig. S5†) chosen

Fig. 2 TEM micrographs corresponding to the NaBi$(MoO_4)_2$@PAA samples with different Eu^{3+} contents.

This journal is © the Partner Organisations 2023

Inorg. Chem. Front., 2023, **10**, 3202–3212 | **3205**

Table 1 Mean length and mean width (obtained from the histograms shown in Fig. 1b and S1†), hydrodynamic diameter (HD), crystallite size, unit cell parameters (*a*, *b*, and *c*), and unit cell volume (*V*) obtained for the NaBi(MoO₄)₂@PAA samples doped with different amounts of Eu³⁺. The standard deviation of the NP dimensions and the error associated with the unit cell magnitudes are included in parentheses

Eu/(Eu + Bi) (% nominal)	Length (nm)	Width (nm)	HD (nm)	Crystallite size (nm)	$a = b$ (Å)	c (Å)	V (Å³)
0	218 (33)	75 (11)	190	57	5.2963 (3)	11.600 (1)	325.39
5	166 (28)	55 (16)	164	55	5.2950 (3)	11.596 (1)	325.12
10	149 (79)	55 (16)	127	48	5.2935 (2)	11.5826 (8)	324.56
20	68 (45)	25 (12)	68	27	5.2916 (3)	11.567 (1)	323.89
30	39 (20)	19 (18)	55	18	5.2871 (4)	11.549 (1)	322.83

as a representative example. Finally, the europium-doped NPs were also coated with PAA as illustrated in Fig. S6 and S7.†

3.2. Luminescence properties

The excitation spectra recorded for all Eu³⁺-doped NaBi(MoO₄)₂ samples functionalized with PAA (Eu³⁺:NaBi(MoO₄)₂@PAA) and dispersed in water, fixing the emission at the wavelength of the most intense Eu³⁺ emission band (612 nm), are shown in Fig. 3 (top). As observed, irrespective of the Eu content, they consisted of a weak and broad excitation band at $\lambda < 300$ nm along with several narrow emission bands in the 370–550 nm region, the most intense one appearing at 464 nm. The former has been ascribed to the combination of Eu³⁺–O²⁻ and Mo⁶⁺–O²⁻ charge transfer transitions along with

the s–p transition of the Bi³⁺ ion, whereas the latter result from the f–f electronic transitions characteristic of Eu³⁺ as shown in the figure.[14]

The emission spectra of such samples recorded by exciting at the wavelength corresponding to the most intense excitation band (464 nm) are shown in Fig. 3 (bottom). All spectra are similar and show the expected emissions of Eu³⁺ cations, corresponding to the ${}^5D_0-{}^7F_j$ (j = 1, 2, 3, 4) transitions.[14] Moreover, the ${}^5D_0 \rightarrow {}^7F_2$ transition, whose intensity was hypersensitive to the symmetry of the Eu³⁺ ion in the crystal lattice, showed a relative intensity much higher than that corresponding to the ${}^5D_0 \rightarrow {}^7F_1$ transition, which is independent of the local environment of the Eu³⁺ cations. This behavior is as expected when such cations are located at a crystallographic site without an inversion center as is the case of that occupied by Bi³⁺ in the NaBi(MoO₄)₂ lattice (S₄),[27] thus confirming the formation of the Eu-NaBi(MoO₄)₂ solid solution. Fig. 3 (bottom) also reveals that the emission intensity is enhanced when the Eu³⁺ doping level is increased from 5 to 10%, whereas on a further increase of this magnitude, a decrease of the emission intensity occurred. The first effect must be associated with the increase of the emission centers. To explain the second effect, it must be considered that for high Ln³⁺ concentrations, the well-known concentration quenching process involving a decrease of the emission intensity also takes place, which, in our case, seems to be predominant at an Eu³⁺ content ≥20%. The presence of such quenching effects was confirmed by measuring the luminescence lifetimes from the decay curves recorded for the most intense emission of Eu³⁺ (614 nm), upon excitation at 465 nm (Fig. 4). These curves could be fitted to a biexponential function given by eqn (1):

$$I(t) = I_1 \exp(-t/\tau_1) + I_2 \exp(-t/\tau_2) \tag{1}$$

where $I(t)$ is the intensity of luminescence, t is the time after excitation, and τ_i (i = 1, 2) is the decay time of the i component, with initial intensity I_i. Such biexponential behavior has been observed very often for other Ln-based nanophosphors and it has been associated with the presence of two different emission centers, namely the Eu³⁺ cations located in the bulk and those near the surface of NPs. The latter suffer from luminescence quenching by the surface impurities and structural imperfection for which their associated lifetime is shorter, whereas the former are well protected against such quenching sources and their lifetimes are longer. The parameters corresponding to each of these components obtained
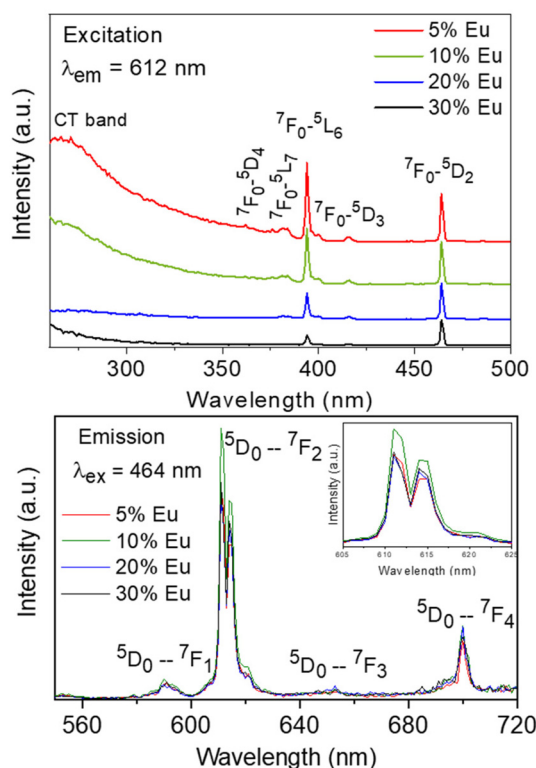

Fig. 3 Excitation (top) and emission (bottom) spectra of the NaBi(MoO₄)₂@PAA samples with different Eu contents. The inset shows an enlargement of the emission spectra in the 605–625 nm wavelength range.

3206 | *Inorg. Chem. Front.*, 2023, **10**, 3202–3212

This journal is © the Partner Organisations 2023

Fig. 4 Decay curves for the NaBi(MoO$_4$)$_2$@PAA samples with different Eu^{3+} contents (λ_{ex} = 465 nm and λ_{em} = 614 nm).

Table 2 Lifetime values of the I_1 (τ_1) and I_2 (τ_2) components and average lifetimes values, $\langle\tau\rangle$, obtained for the NaBi(MoO$_4$)$_2$@PAA samples doped with different amounts of Eu^{3+}

Eu/(Eu + Bi)(% nominal)	τ_1(μs)	I_1 (%)	τ_2 (μs)	I_2 (%)	$\langle\tau\rangle$ (μs)
5	240	34.3	700	65.7	630
10	250	52.9	590	47.1	480
20	180	38.5	510	61.5	450
30	140	39.2	380	60.8	334
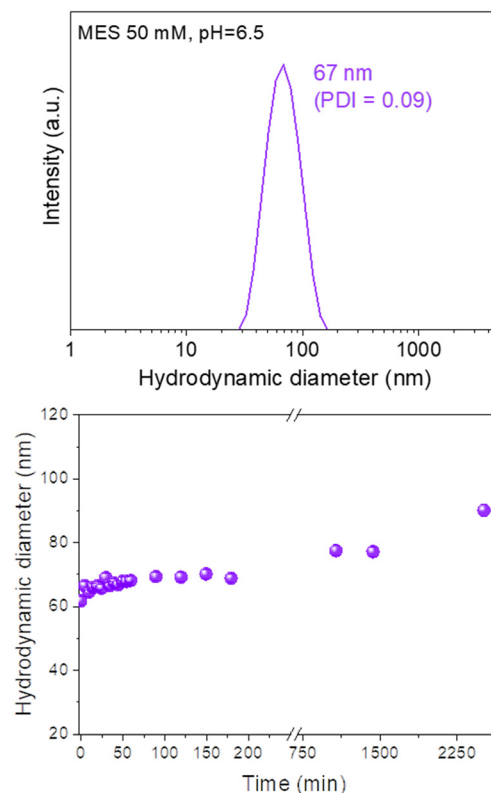
Fig. 6 DLS curve (top) and the evolution of the mean hydrodynamic diameter *vs.* time (bottom) for Eu(20%):NaBi(MoO$_4$)$_2$@PAA NPs suspended in MES medium (pH = 6.5). PDI values were < 0.1 in all cases.
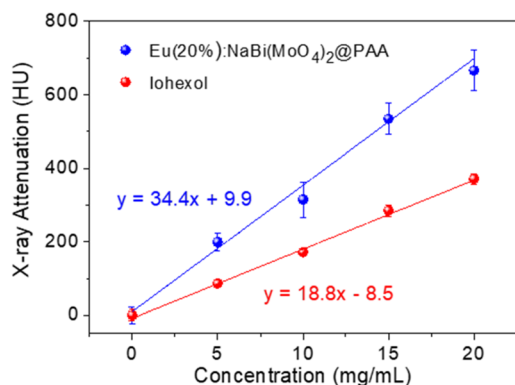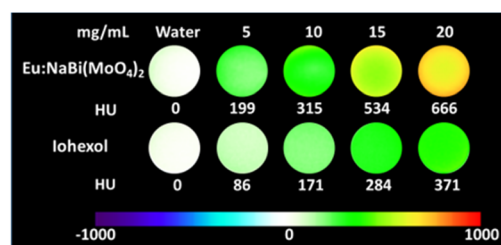

Fig. 5 X-ray attenuation phantom images (top), and X-ray attenuation values in Hounsfield unit (HU) plotted *vs.* the contrast agent concentration (bottom), obtained for iohexol solutions and Eu(20%):NaBi(MoO$_4$)$_2$@PAA NP suspensions having different contrast agent concentrations.
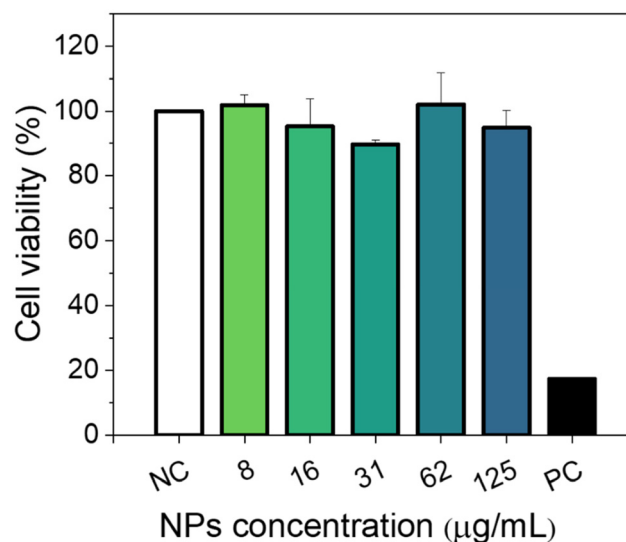

Fig. 7 Viability of MIA-PaCa-2 cells incubated with different concentrations of Eu(20%):NaBi(MoO$_4$)$_2$@PAA nanoparticles for 24 h. Data are represented as mean + standard error of the mean. Values of n = 2 independent experiments are given, with 3 replicates per experiment. Statistical analysis was done by one-way ANOVA analysis followed by Dunnet's multiple comparison test (**p < 0.01) and compared with the negative control (NC).

from the fitting are shown in Table 2, which also includes the average decay times, $\langle \tau \rangle$, obtained according to eqn (2):

$$\langle \tau \rangle = \frac{\int_{t_0}^{t_f} tI(t)\mathrm{d}t}{\int_{t_0}^{t_f} I(t)\mathrm{d}t} = \left(\tau_1^2 I_1 + \tau_2^2 I_2\right)/(\tau_1 I_1 + \tau_2 I_2) \qquad (2)$$

As observed, the values of τ decreased on increasing the Eu^{3+} doping level indicating the presence of the concentration quenching effect, and the phosphor with the most efficient luminescence is that having the lowest Eu^{3+} content. Nevertheless, the NP size for this sample is above 100 nm and therefore does not meet the size criteria for *in vivo* bioimaging. For this reason, for the experiments shown in the next sections, we selected the sample doped with 20% Eu^{3+}, whose

mean size lies well within the nanometer range (Table 1) while keeping a high luminescence intensity, close to that of the most efficient phosphor (Fig. 3).

3.3. X-ray attenuation properties

The X-ray attenuation phantom images obtained for dispersions having different concentrations of Eu(20%):NaBi$(MoO_4)_2$@PAA NPs in water as well as those corresponding to iohexol, which is the iodine-containing commercial CT CA selected for comparison, are presented in Fig. 5 (top). This figure shows the change of the image contrast on varying the amount of CA contained in the suspensions, which manifests that our NPs behave as a CT CA. Additional information is

Fig. 8 Optical microscopy images to evaluate the morphology of Mia-PaCa-2 cells incubated with different concentrations of NaBi$(MoO_4)_2$@PAA nanoparticles for 24 h. The right bottom scale applies to all micrographs.

obtained by plotting the X-ray attenuation values (in Hounsfield units, HU) *vs.* the CA content (Fig. 5, bottom). This plot shows that in all cases, the X-ray attenuation produced by our NPs is much higher than that corresponding to iohexol solutions containing the same amount of CA. This finding clearly indicates the superior capability of our Eu(20%):NaBi(MoO$_4$)$_2$@PAA NPs to act as a CA for CT imaging when compared with the commercial agent, which must be ascribed to the higher atomic number of Bi (83) cations as compared with that of I (53).

3.4.   Colloidal stability in physiological medium

The colloidal stability of our Eu(20%):NaBi(MoO$_4$)$_2$@PAA NPs in physiological media was analyzed using a NP suspension in an MES solution (pH = 6.5), which is a physiological buffer usually tested for this purpose.[25] The HD value obtained from DLS measurements for this suspension (Fig. 6, top) was very similar (67 nm, PDI = 0.09) to the mean diameter measured from the TEM micrographs (68 × 25 nm). Such behavior demonstrates that the NPs are well dispersed in MES medium. Moreover, no important changes in the HD values were noticed after aging such a suspension for different periods of time up to 2520 min (42 h) (Fig. 6, bottom) indicating a high colloidal stability in MES medium and that, our NPs are suitable for *in vivo* applications.

3.5.   Cytotoxicity

Cytotoxicity experiments were conducted using MIA-PaCa-2 cells as a model. Different parameters were evaluated including mitochondrial activity (Fig. 7) and cell morphology (Fig. 8). As shown in Fig. 7, no statistical difference in cell viability between cells incubated with and without NPs was obtained. Furthermore, a high cell viability (>90%) was observed for NP concentrations as high as 125 μg mL^{-1}. Additionally, no appreciable changes in the morphology of the cells were detected after they were exposed to NPs in a concentration of

up to 125 μg mL^{-1} (Fig. 8). These preliminary results indicate the suitability of our Eu(20%):NaBi(MoO$_4$)$_2$@PAA NPs as a promising tool for bioimaging applications.

3.6.   *In vivo* toxicity

In vivo toxicity was evaluated using the *C. elegans* wild-type strain, N2. The worms were fed with different Eu(20%):NaBi

Fig. 10 Viability of N2 worms incubated at 20 °C with different concentrations of Eu(20%):NaBi(MoO$_4$)$_2$@PAA NPs for 24 h. Data are normalized according to the control (worms in Milli-Q water with no nanoparticle exposure) considered as 100%. Data are represented as the mean + standard error of the mean, values of n = 3 independent experiments are given (for 1000 μg mL^{-1}, n = 2), with 48 replicates per experiment. Statistical analysis was done by Kruskal−Wallis analysis followed by Dunn's multiple comparison test (****p < 0.0001) and compared with the control.

Fig. 9 Localization of Eu(20%):NaBi(MoO$_4$)$_2$@PAA NPs (in red) through the intestine of the worm after 24 h exposition. Composition of 4 pictures merging white field and fluorescence microscopy.

This journal is © the Partner Organisations 2023

Inorg. Chem. Front., 2023, **10**, 3202–3212 | **3209**

$(MoO_4)_2$@PAA concentrations in aqueous dispersion for 24 h at 20 °C. It is well known that *C. elegans*, during feeding, pumps liquids by rhythmic contractions of the pharynx into the lumen of the intestine.[28] To test whether the nematode could ingest our NPs through this process, we used confocal microscopy for worms treated with 500 μg mL^{-1} Eu(20%):NaBi $(MoO_4)_2$@PAA as an example. As observed in Fig. 9, red spots corresponding to the luminescence of our NPs were detected through the intestine of the nematode after treatment indicating the ingestion of NPs.

To analyse the potential toxicity after ingestion, an endpoint lethality test from 0 to 1000 μg mL^{-1} of Eu(20%):NaBi $(MoO_4)_2$@PAA was done (Fig. 10), observing that no significant lethality was present up to a NP concentration of 100 μg mL^{-1}. A small but significant effect was, however, detected at a much higher concentration (>500 μg mL^{-1}), which has also been observed for NPs of different compositions such as Au,[19] Ag,[29] or iron oxide.[30] This kind of toxicity could be due to a mechanical effect, considering that this concentration is quite high and that the NPs seem to aggregate inside the intestine lumen (Fig. 9), which could affect viability. This idea would be supported by the absence of cytotoxicity found for human cells at a concentration of up to 125 μg mL^{-1}. Therefore, it can be concluded that in this concentration range, which is the one required for most *in vivo* applications, the Eu(20%): $(MoO_4)_2$@PAA NPs are also safe for the here-considered *C. elegans* model.

4. Conclusions

Uniform Eu^{3+}-doped NaBi$(MoO_4)_2$ nanoparticles functionalized with polyacrylic acid (Eu:NaBi$(MoO_4)_2$@PAA) have been obtained using a one-pot procedure involving a homogenous precipitation reaction at 120 °C for 20 h, from solutions in ethylene glycol/water medium containing appropriate concentrations of bismuth nitrate, europium nitrate, sodium molybdate, and polyacrylic acid. The shape of these nanoparticles was ellipsoidal and their size could be varied within the nanometer range by varying the Eu^{3+} doping level (in the 5–30% Eu/(Eu + Bi) molar ratio). In all cases, the nanoparticles consisted of tetragonal NaBi$(MoO_4)_2$. The luminescence properties of such nanoparticles have been comparatively evaluated as a function of the Eu^{3+} doping level, finding, in all cases, an intense red emission when excited at 465 nm. The Eu(20%): NaBi$(MoO_4)_2$@PAA nanoparticles, selected as a case of study, also showed better X-ray attenuation properties than iohexol (a commercial CT contrast agent), which is associated with their constituting Bi^{3+} cation. Moreover, these nanoparticles could be well dispersed in water and 2-*N*-morpholinoethanesulfonic acid monohydrate medium (pH = 6.5), which is frequently used as a physiological pH simulator, as revealed by their hydrodynamic diameter values. Finally, cell viability (MIA-PaCa-2 cells) and *in vivo* toxicity (nematode *Caenorhabditis elegans* model) experiments demonstrated that they were nontoxic up to a NP concentration of 100 μg mL^{-1},

which is within the range required for most *in vivo* applications. Because of these properties, the developed Eu(20%): NaBi$(MoO_4)_2$ nanoparticles are excellent candidates for their use as bimodal probes for luminescence imaging and X-ray computed tomography.

Author contributions

Conflicts of interest

There are no conflicts to declare.

Acknowledgements

References

1 N. O. Núñez, E. Gómez-González, R. M. Calderón-Olvera, A. I. Becerro, G. Colón and M. Ocaña, NaY$(MoO_4)_2$-based nanoparticles: synthesis, luminescence and photocatalytic properties, *Dalton Trans.*, 2021, **50**, 16539–16547.

2 T. Wang, S. Wang, H. Zhang, X. Zou and W. Hu, Tm^{3+}-Dy^{3+}-Eu^{3+} tri-doped transparent glass-ceramics containing NaY $(MoO_4)_2$ crystal phase: Preparation, energy transfer, warm white light emitting, *Opt. Mater.*, 2020, **104**, 109851.

3210 | *Inorg. Chem. Front.*, 2023, **10**, 3202–3212

This journal is © the Partner Organisations 2023

3 Y. Ding, J. Liu, M. Zeng, X. Wang, J. Shi, W. Wang, Y. Miao and X. Yu, Tunable morphologies, multicolor properties and applications of RE^{3+} doped $NaY(MoO_4)_2$ nanocrystals via a facile ligand-assisted reprecipitation process, *Dalton Trans.*, 2018, **47**, 8697–8705.

4 V. A. Morozov, S. M. Posokhova, S. Y. Istomin, D. V. Deyneko, A. A. Savina, B. S. Redkin, N. V. Lyskov, D. A. Spassky, A. A. Belik and B. I. Lazoryak, $KTb(MoO_4)_2$ Green Phosphor with K^+-Ion Conductivity: Derived from Different Synthesis Routes, *Inorg. Chem.*, 2021, **60**, 9471–9483.

5 A. Li, D. Xu, H. Lin, S. Yang, Y. Shao and Y. Zhang, $NaGd(MoO_4)_2$ nanocrystals with diverse morphologies: controlled synthesis, growth mechanism, photoluminescence and thermometric properties, *Sci. Rep.*, 2016, **6**, 31366.

6 V. A. Morozov, S. M. Posokhova, D. V. Deyneko, A. A. Savina, A. V. Morozov, O. A. Tyablikov, B. S. Redkin, D. A. Spassky, J. Hadermann and B. I. Lazoryak, Influence of annealing conditions on the structure and luminescence properties of $KGd_{1-x}Eu_x(MoO_4)_2$ ($0 \leq x \leq 1$), *CrystEngComm*, 2019, **21**, 6460–6471.

7 M. Laguna, N. O. Núñez, V. Rodríguez, E. Cantelar, G. Stepien, M. L. García, J. M. de la Fuente and M. Ocaña, Multifunctional Eu-doped $NaGd(MoO_4)_2$ nanoparticles functionalized with poly(L-lysine) for optical and MRI imaging, *Dalton Trans.*, 2016, **45**, 16354–16365.

8 C. Zaldo, M. D. Serrano, X. Han, C. Cascales, M. Cantero, L. Montoliu, E. Arza, V. R. Caiolfa and M. Zamai, Efficient up-conversion in $Yb:Er:NaT(XO_4)_2$ thermal nanoprobes. Imaging of their distribution in a perfused mouse, *PLoS One*, 2017, **12**(5), e0177596.

9 A. Escudero, A. I. Becerro, C. Carrillo-Carrión, N. O. Núñez, M. V. Zyuzin, M. Laguna, D. González-Mancebo, M. Ocaña and W. J. Parak, Rare earth based nanostructured materials: synthesis, functionalization, properties and bioimaging and biosensing applications, *Nanophotonics*, 2017, **6**, 881–921.

10 M. Laguna, N. O. Núñez, A. I. Becerro, G. Lozano, M. Moros, J. M. de la Fuente, A. Corral, M. Balcerzyk and M. Ocaña, Synthesis, functionalization and properties of uniform europium-doped sodium lanthanum tungstate and molybdate ($NaLa(XO_4)_2$, X = Mo,W) probes for luminescent and X-ray computed tomography bioimaging, *J. Colloid Interface Sci.*, 2019, **554**, 520–530.

11 S. Zhao, R. R. Tian, B. Q. Shao, Y. Feng, S. W. Yuan, L. P. Dong, L. Zhang, Z. X. Wang and H. P. You, One-pot synthesis of Ln^{3+}-doped porous $BiF_3@PAA$ nanospheres for temperature sensing and pH-responsive drug delivery guided by CT imaging, *Nanoscale*, 2020, **12**, 695–702.

12 Pushpendra, R. K. Kunchala, R. Kalia and B. S. Naidu, Excitation dependent visible and NIR photoluminescence properties of Er^{3+}, Yb^{3+} co-doped $NaBi(MoO_4)_2$ nanomaterials, *RSC Adv.*, 2020, **10**, 14525–14530.

13 J. Xie, L. Cheng, H. Tang, X. Yu, Z. Wang, X. Mi, Q. Liu and X. Zhang, Synthesis and photoluminescence properties of NUV-excited $NaBi(MoO_4)_2$: Sm^{3+} phosphors for white light emitting diodes, *Opt. Laser Technol.*, 2022, **147**, 107659.

14 Pushpendra, R. K. Kunchala, S. N. Achary and B. S. Naidu, $NaBi_{0.9}Eu_{0.1}(MoO_4)_2$ Nanomaterials: Tailoring the Band Gap and Luminescence by La^{3+} Substitution for Light-Emitting Diodes, *ACS Appl. Nano Mater.*, 2019, **2**, 5527–5537.

15 Pushpendra, R. K. Kunchala, S. N. Achary, A. K. Tyagi and B. S. Naidu, Rapid, Room Temperature Synthesis of Eu^{3+} Doped $NaBi(MoO_4)_2$ Nanomaterials: Structural, Optical, and Photoluminescence Properties, *Cryst. Growth Des.*, 2019, **19**, 3379–3388.

16 Pushpendra, R. K. Kunchala, R. Kalia and B. S. Naidu, Upconversion luminescence properties of $NaBi(MoO_4)_2$: Ln^{3+}, Yb^{3+} (Ln = Er, Ho) nanomaterials synthesized at room temperature, *Ceram. Int.*, 2020, **46**, 18614–18622.

17 Y. Gan, W. Liu, W. Zhang, W. Li, Y. Huang and K. Qiu, Effects of Gd^{3+} codoping on the enhancement of the luminescent properties of a $NaBi(MoO_4)_2:Eu^{3+}$ red-emitting phosphors, *J. Alloys Compd.*, 2019, **784**, 1003–1010.

18 S. Jiang, K. Y. Win, S. Liu, C. P. Teng, Y. Zheng and M.-Y. Han, Surface-functionalized nanoparticles for biosensing and imaging-guided therapeutics, *Nanoscale*, 2013, **5**, 3127–3148.

19 L. González-Moragas, P. Berto, C. Vilches, R. Quidant, A. Kolovou, R. Santarella-Mellwig, Y. Schwab, S. Sturzenbaum, A. Roig and A. Laromaine, In vivo testing of gold nanoparticles using the Caenorhabditis elegans model organism, *Acta Biomater.*, 2017, **53**, 598–609.

20 L. Alvino, M. Pacheco-Herrero, Ál. López-Lorente, Z. Quiñones, S. Cardenas and Z. Isabel González-Sánchez, Toxicity evaluation of barium ferrite nanoparticles in bacteria, yeast and nematode, *Chemosphere*, 2020, **254**, 126786.

21 T. Stiernagle, Maintenance of C. elegans, in *WormBook : the online review of C. elegans biology*, 2006, 1–11.

22 A. Waskowska, L. Gerward, J. S. Olsen, M. Maczka, T. Lis, A. Pietraszko and W. Morgenroth, Low-temperature and high-pressure structural behaviour of $NaBi(MoO_4)_2$ - an X-ray diffraction study, *J. Solid State Chem.*, 2005, **178**, 2218–2224.

23 T. Mosmann, Rapid colorimetric assay for cellular growth and survival - application to proliferation and cyto-toxicity assays, *J. Immunol. Methods*, 1983, **65**, 55–63.

24 E. Arroyo, B. Torres-Herrero, J. M. de la Fuente, M. Ocaña and A. I. Becerro, Highly uniform $Y_3Al_2Ga_3O_{12}$-based nanophosphors for persistent luminescence bioimaging in the visible and NIR regions, *Inorg. Chem. Front.*, 2022, **9**, 2454–2461.

25 N. O. Núñez, S. Rivera, D. Alcántara, J. M. de la Fuente, J. García-Sevillano and M. Ocaña, Surface modified Eu: $GdVO_4$ nanocrystals for optical and MRI imaging, *Dalton Trans.*, 2013, **42**, 10725–10734.

26 R. Buonsanti and D. J. Milliron, Chemistry of Doped Colloidal Nanocrystals, *Chem. Mater.*, 2013, **25**, 1305–1317.

This journal is © the Partner Organisations 2023

Inorg. Chem. Front., 2023, **10**, 3202–3212 | **3211**

27 C. Cascales, A. M. Blas, M. Rico, V. Volkov and C. Zaldo, The optical spectroscopy of lanthanides R^{3+} in $ABi(XO_4)2$ (A = Li, Na; X = Mo, W) and $LiYb(MoO_4)_2$ multifunctional single crystals: Relationship with the structural local disorder, *Opt. Mater.*, 2005, **27**, 1672–1680.

28 L. Avery and Y.-J. You, C. elegans feeding, in *WormBook : the online review of C. elegans biology*, 2012, 1–23.

29 S. W. Kim, S.-H. Nam and Y.-J. An, Interaction of Silver Nanoparticles with Biological Surfaces of Caenorhabditis elegans, *Ecotoxicol. Environ. Saf.*, 2012, **77**, 64–70.

30 Q. Wu, Y. Li, M. Tang and D. Wang, Evaluation of Environmental Safety Concentrations of DMSA Coated Fe_2O_3-NPs Using Different Assay Systems in Nematode Caenorhabditis elegans, *PLoS One*, 2012, **7**(8), e43729.

3212 | *Inorg. Chem. Front.*, 2023, **10**, 3202–3212

This journal is © the Partner Organisations 2023